

# A spectral-structural characterization of European temperate, hemiboreal and boreal forests

Miina Rautiainen<sup>1</sup>, Aarne Hovi<sup>1</sup>, Daniel Schraik<sup>1,2</sup>, Jan Hanuš<sup>3</sup>, Petr Lukeš<sup>3</sup>, Zuzana Lhotáková<sup>4</sup>, Lucie Homolová<sup>3</sup>

<sup>1</sup>School of Engineering, Aalto University, Espoo, 00076, Finland

<sup>2</sup>Natural Resources Institute Finland, Helsinki, 00790, Finland

<sup>3</sup>CzechGlobe Global Change Research Institute of the Czech Academy of Sciences, Brno, 60300, Czech Republic

<sup>4</sup>Department of Experimental Plant Biology, Charles University, Prague, 12843, Czech Republic

*Correspondence to:* Miina Rautiainen (miina.a.rautiainen@aalto.fi)

**Abstract.** Radiative transfer models of vegetation play a crucial role in the development of remote sensing methods by providing a theoretical framework to explain how electromagnetic radiation interacts with vegetation in different spectral regions. A limiting factor in model development has been the lack of sufficiently detailed ground reference data on both structural and spectral characteristics of forests needed for testing and validating the models. In this data description paper, we present a dataset on the structural and spectral properties of 58 stands in temperate, hemiboreal and boreal European forests. It is specifically designed for the development and validation of radiative transfer models for forests but can also be utilized in other remote sensing studies. It comprises detailed data on forest structure based on forest inventory measurements, terrestrial and airborne laser scanning, and digital hemispherical photography. Furthermore, the data include spectral properties of the same forests at multiple scales: reflectance spectra of tree leaves and needles (based on laboratory measurements), forest floor (based on in situ measurements) and entire stands (based on airborne measurements), as well as transmittance spectra of tree leaves and needles and entire tree canopies (based on laboratory and in situ measurements, respectively). We anticipate that these data will have wide use in testing and validating radiative transfer models for forests and in the development of remote sensing methods for vegetation. The data can be accessed at:

Hovi et al. 2024a, <https://doi.org/10.23729/9a8d90cd-73e2-438d-9230-94e10e61adc9> (for laboratory and field data) and

Hovi et al. 2024b, <https://doi.org/10.23729/c6da63dd-f527-4ec9-8401-57c14f77d19f> (for airborne data).

## 1 Introduction

Remote sensing of vegetation, and forests in particular, has experienced significant growth in recent years (e.g., Fassnacht et al., 2024) due to advancements in sensor technology, data processing and interpretation techniques, and new satellite missions (such as PRISMA, EnMAP, CHIME, SBG). At a global level, remote sensing can provide information about pressing global issues such as the connections between climate change and vegetation dynamics (e.g., Piao et al., 2020) and support for biodiversity conservation (e.g., Pettorelli et al., 2016). Furthermore, at finer spatial scales, optical remote sensing allows detailed and accurate monitoring of, for example, vegetation productivity, diversity and health (e.g., Kooistra et al., 2024; Hernández-Clemente et al., 2019).

Radiative transfer (RT) models of vegetation play a crucial role in the development of remote sensing methods by providing a theoretical framework to explain how electromagnetic radiation interacts with vegetation in different spectral regions (Ross, 1981; Myneni & Ross, 1991). Based on mathematical formulations, these models allow us to understand and quantify the complex interactions between radiation and canopy components, such as leaves, and stems, and the underlying soil (Liang, 2004). By modeling the radiative transfer processes, it is possible to explain the spectral signatures observed by remote sensing instruments under different environmental and illumination conditions, or support future sensor design and planning of data collection strategies (e.g., Vicent et al., 2015).

42 RT models and other physically-based canopy reflectance and transmittance models have been developed for over three  
43 decades. For forests, these models (e.g., Gastellu-Etchegorry et al., 1996; North, 1996; Kuusk & Nilson, 2000; Leblanc &  
44 Chen, 2001) are often more complicated, and require a larger number of input variables than models for other vegetation  
45 ecosystems (e.g., Jacquemoud et al. 2009; Verhoef et al., 1984) due to the complex tree canopy architecture and subsequent  
46 multiple interactions of photons both within and between canopy elements, and between forest floor and the canopy (e.g.,  
47 Stenberg et al., 2008). Even though there are modeling approaches that require a smaller number of input variables for forests  
48 (Stenberg et al., 2016), a limiting factor in model development has been the lack of extensive or sufficiently detailed ground  
49 reference data on both structural and spectral characteristics of forests needed for testing and validating the models. This lack  
50 of data affects both model developers and larger scientific frameworks, such as the RAdiation transfer Model Intercomparison  
51 (RAMI) initiative (Gobron et al., 2023). While structural data on forests (e.g., tree height, crown length, number of trees per  
52 ground area, canopy cover, leaf area index) are commonly available from sources such as forest inventory databases, spectral  
53 data on forest components (e.g., leaf or forest floor reflectance and/or transmittance spectra) are less frequently accessible. In  
54 addition, some structural properties (e.g., clumping index) that are relevant for RT models are also not commonly available  
55 but can be derived from detailed structural measurements.

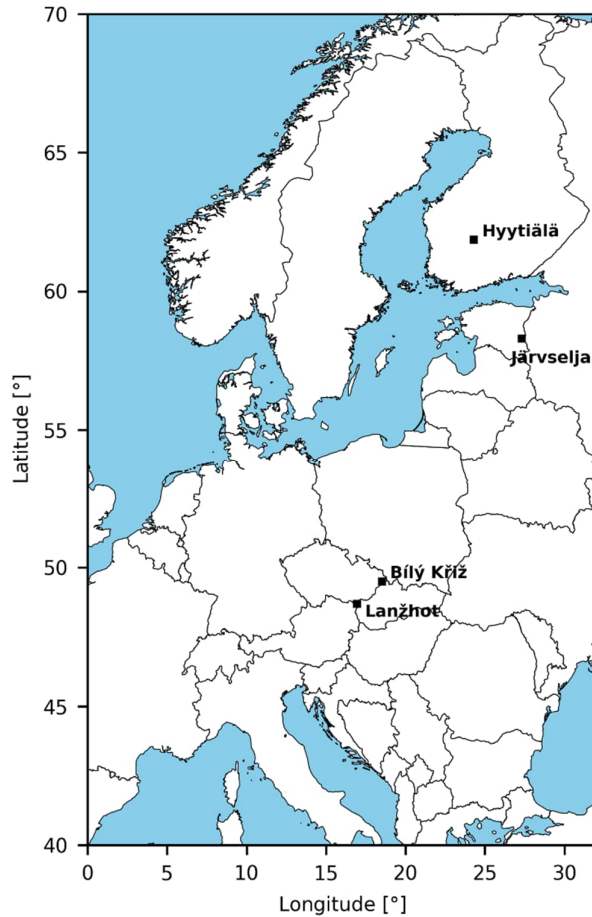
56 To date, major efforts in collecting ground reference data that can be used in radiative transfer models for forests have focused  
57 on the North American continent. For instance, projects like the National Ecological Observatory Network (NEON) (NEON,  
58 2024) and the Boreal Ecosystem-Atmosphere Study (BOREAS) (Sellers et al., 1997) offer input data for developing RT  
59 modeling for forests. While these initiatives have primarily aimed to understand ecosystem dynamics, their datasets also  
60 include key variables needed for RT models. For testing and validating forest RT models in European forests, there is only a  
61 small number of datasets that include the necessary structural and spectral information across various scales (e.g., Kuusk et  
62 al., 2009; Widlowski et al., 2015; Schneider et al., 2017; Liu et al., 2023). Furthermore, these datasets are limited in size,  
63 containing information on only a few forest stands. Even though various solutions have been suggested to overcome the lack  
64 of input data for RT models by using data from multiple sources (e.g., Malenovský et al., 2019), the lack of missing primary  
65 data persists. In addition to having to collect the data from multiple sources representing different time periods or geographical  
66 locations, these datasets are often not openly available according to FAIR (Findable, Accessible, Interoperable, Reusable) Data  
67 principles (Wilkinson et al., 2016).

68 In this data description paper, we present a unique, open dataset on the structural and spectral properties of 58 stands in  
69 temperate, hemiboreal and boreal European forests collected in a project funded by the European Research Council. The  
70 dataset is specifically designed for the development and validation of radiative transfer models for forests but can also be  
71 utilized in other remote sensing studies. It comprises detailed information on forest structure based on forest inventory  
72 measurements, terrestrial and airborne laser scanning, and digital hemispherical photography. Furthermore, the dataset  
73 includes spectral properties of the forests at multiple scales: reflectance spectra of tree leaves and needles (based on laboratory  
74 measurements), forest floor (based on in situ measurements) and entire stands (based on airborne measurements), as well as  
75 transmittance spectra of tree leaves and needles and entire tree canopies (based on laboratory and in situ measurements,  
76 respectively). For distributing the data, we selected open, widely available formats. The dataset follows the FAIR principles.

77 **2 Data collection**

78 **2.1 Study sites**

79 We collected data from 58 forest stands representing different forest structures and species compositions in temperate,  
80 hemiboreal and boreal forests of Europe during summers 2019-2021 (Table 1, Fig. 1). The sites in Finland and the Czech  
81 Republic (Hyytiälä, Lanžhot, Bílý Kříž) are part of the Integrated Carbon Observation System (ICOS) which means that time  
82 series of meteorological and other ecosystem data are also openly available. The site in Estonia (Järvselja) also has a tower  
83 system for measuring variables related to atmosphere-biosphere interactions, and the data are available, per request from the  
84 tower manager. We have summarized information on the study sites in Table 1 and we provide a short verbal description of  
85 them in the following text.



86

87 **Figure 1.** A map showing the locations of the study sites.

88 Our boreal study site was located in Finland, Hyytiälä (61°51'N, 24°18'E), and is a moderately flat (130–200 m a.s.l.) area  
89 dominated by coniferous tree species. The forest floor is dominated by dwarf shrubs, graminoids, mosses or lichens. Bare soil  
90 is rarely visible. Field measurements in Hyytiälä were conducted during 2019 and 2021.

91 Our hemiboreal site was located in Estonia, Järvselja (58°17'N, 27°19'E), and is a flat (30-45 m a.s.l.) area with mixed  
92 broadleaved and coniferous forests. The forest floor is dominated by shrubs, dwarf shrubs, graminoids and mosses. Bare soil  
93 is rarely visible. Field measurements in Järvselja were conducted during 2020.

94 Our temperate study sites, Lanžhot and Bílý Kříž, were located in the Czech Republic. Lanžhot (48°41'N, 16°57'E), is a  
 95 temperate broadleaf-dominated floodplain forest area (ca 150 m a.s.l.). The forest floor is sparsely covered by graminoids and  
 96 shrubs, and decomposed plant materials (or bare soil) is commonly visible due to a high game density. Bílý Kříž (49°30'N,  
 97 18°32'E), on the other hand, is a temperate coniferous mountain forest area (700–950 m a.s.l.) where the forest floor is  
 98 dominated by dwarf shrubs, graminoids and mosses. Field measurements in the Czech sites were conducted during 2019.  
 99

100 **Table 1.** Summary of the study plots and measurement campaigns.

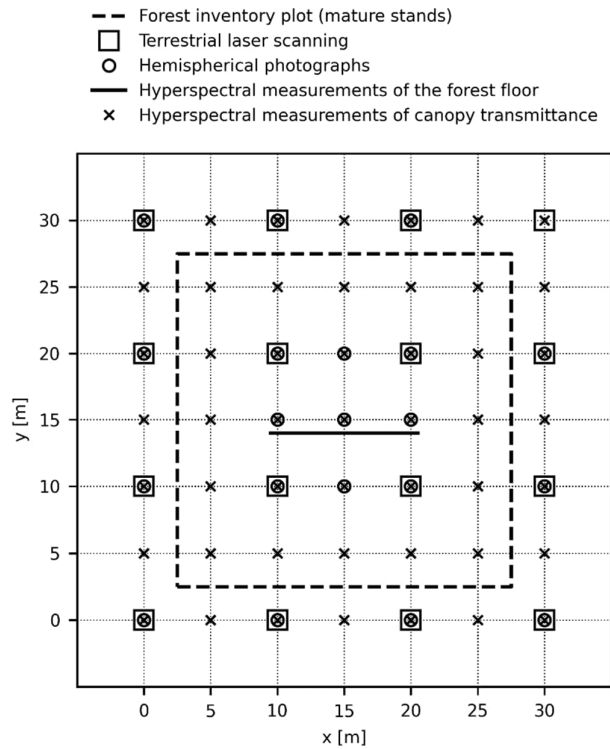
	<b>Hyytiälä</b>	<b>Järvelja</b>	<b>Bílý Kříž</b>	<b>Lanžhot</b>
Forest biome	boreal	hemiboreal	temperate	temperate
Number of plots	28	13	7	10
Mean (and range) of tree height [m]	20 (6 – 34)	19 (4 – 39)	23 (5 – 43)	31 (18 – 40)
Mean basal area (and its range) [m <sup>2</sup> ha <sup>-1</sup> ]	23 (4 – 46)	19 (4 – 51)	34 (3 – 66)	33 (14 – 60)
Effective plant area index [m <sup>2</sup> m <sup>-2</sup> ]	1.9 (0.1 – 3.9)	2.5 (0.4 – 6.3)	2.9 (0.4 – 4.7)	3.7 (2.1 – 5.3)
Time of field campaign	17 June – 26 July 2019, 8 July - 5 August 2021	24 June – 19 July 2020	16 – 29 September 2019	3 – 12 September 2019
Time of airborne campaign (date, local time)	13 July 2019, 08:57-10:21	15 July 2019, 12:57-14:07	4 September 2019, 11:01-11:07	4 September 2019, 12:14-12:22
Solar zenith angle during airborne measurements	51-60°	37-38°	47-48°	42°

101

102 **2.2 Overview of measurement campaigns**

103 We established 28 plots in Hyytiälä, 13 in Järvelja, 10 in Lanžhot, and 7 in Bílý Kříž (Fig. 2). Each plot was located within a  
 104 homogeneous forest stand with a minimum distance of 30 m from the plot center to the stand border, to ensure that uncertainties  
 105 in geolocation would not impact the interpretation of commonly used medium spatial resolution optical satellite data. The  
 106 same sampling and measurement protocols were applied in collecting field data in all study sites. Photographs from the  
 107 measurement campaigns are available in Appendix A (Fig. A1) and in the published datasets. Note that we apply the reflectance  
 108 terminology outlined by Schaepman-Strub et al. (2006) for the field and laboratory spectral measurements described in this  
 109 paper.

110 In all plots, we carried out forest inventory (Sect. 2.3.1) and terrestrial laser scanning (Sect. 2.3.2), took hemispherical  
 111 photographs of the tree canopy (Sect. 2.3.3) and conducted spectral measurements and estimation of vegetation fractional  
 112 cover of the forest floor layer (Sect. 2.3.4). In addition, we measured the spectral transmittance of tree canopies in a subset of  
 113 plots (Sect. 2.3.5) and measured the reflectance and transmittance spectra of the foliage of dominant tree species in all study  
 114 sites (Sect. 2.3.6). The illumination and view geometries of the sensors during the field measurements are provided in Appendix  
 115 A (Fig. A2). An airborne measurement campaign in all study sites was conducted to obtain contemporaneous hyperspectral  
 116 (Sect. 2.4.1) and laser scanning data (Sect. 2.4.2). The same aircraft and instrumentation were used for the acquisition of  
 117 airborne data in all measurement campaigns. The datasets are provided by Hovi et al. 2024a and Hovi et al. 2024b.



118  
 119 **Figure 2.** A diagram showing the sampling design for field measurements described in Section 2.3.

## 120 2.3 Field datasets

### 121 2.3.1 Forest inventory

122 We conducted forest inventory measurements to obtain detailed information on the tree species and stand structure and took  
123 photographs of each plot at six fixed locations to provide an overview of the forests for data users. **The fixed locations were**  
124 **all four corners of the plot and in the center of the plot (in two different directions)**. Forest inventory was carried out with  
125 distinct protocols for mature stands ( $D > 10$  cm) and young stands ( $D < 10$  cm), categorized based on the average diameter at  
126 1.3 m height ( $D$ ) for trees. For simplicity, we refer to stands with  $D > 10$  cm as mature stands and those with  $D < 10$  cm as  
127 young stands.

128 In mature stands (**number of plots,  $n = 44$** ), a tree-wise inventory was performed within a rectangular area measuring  $25\text{ m} \times$   
129  $25\text{ m}$  (Fig. 2). The diameter at 1.3 m height was measured using a caliper, and the tree species were identified for every tree  
130 exceeding a predetermined diameter threshold. The thresholds were determined in relation to the average tree height in the  
131 plot ( $h$ ) and were as follows: 8 cm if  $h > 16$  m, 5 cm if  $10\text{ m} \leq h \leq 16$  m, and 2.5 cm if  $h < 10$  m. Tree height was measured  
132 with a Vertex ultrasonic hypsometer for two trees (median trees of thickest 10% of trees) in each plot. These plots had 16  
133 terrestrial laser scanning (TLS) points (see Section 2.3.2).

134 In young stands ( $n = 6$ ), 16 circular sub-plots were measured, arranged in a  $4 \times 4$  grid with a 10 m distance between grid points  
135 (see TLS grid in Fig. 2). The area of each sub-plot was  $25\text{ m}^2$  (i.e., had a radius of 2.82 m). Within each sub-plot, the number  
136 of trees per species, along with the diameter and height of a median tree per species, were measured. These plots had one  
137 terrestrial laser scanning (TLS) point (see Section 2.3.2).

138 An exception to the forest inventory protocol was made only in Hyytiälä for the plots ( $n = 8$ ) measured in 2021, where relascope  
139 sampling was used to determine whether a tree belonged to the plot or not. Diameter at 1.3 m height was measured for all  
140 sampled trees, and tree height was measured for the median tree per species. These plots had one terrestrial laser scanning  
141 (TLS) point (see Section 2.3.2).

142  
143 Descriptive forest characteristics were derived from the forest inventory data for each study plot. These include: number of  
144 stems per hectare, basal area, tree species proportions, and tree dimensions (i.e., stem diameter and tree height). More accurate  
145 description of the calculation of these variables is provided in the readme file of the data. **In forest inventory measurements,**  
146 **typical uncertainties (standard deviation) for diameter at breast height and tree height are 0.3 cm and 0.5 m, respectively**  
147 **(Luoma et al. 2017).**

148

### 149 2.3.2 Terrestrial laser scanning (TLS)

150 We collected TLS data that can be used to characterize the 3D geometry of the forest canopies in all plots, comprising a total  
151 of ~2800 individual trees. The Leica P40 ScanStation, utilized in our study, operates at a wavelength of 1550 nm. It has a 6  
152 mm beam diameter at the source and a 0.23 mrad beam divergence. The scan resolution equaled the beam divergence (i.e.,  
153 0.23 mrad or around  $0.013^\circ$ ). The only exceptions to this were the measurements 1) in Hyytiälä in 2021 ( $n = 8$ ), and 2) in  
154 young stands in Järvelja ( $n = 4$ ) where the scan resolution was 0.31 mrad ( $0.018^\circ$ ). These exceptions are clearly labelled in  
155 the dataset.

156 There were two alternative sampling strategies for collecting TLS data. The choice of sampling approach was based on stand  
157 density at a height of 1-2 m above ground to avoid occlusion of co-registration targets, and time constraints. In 44 plots, TLS

158 scans were conducted at 16 grid points (Fig. 2), corresponding to the "mature" forest category described in Section 2.3.1. In  
159 14 plots, TLS scans were conducted only at a single location (at the center of the plot, Fig. 2).

160 Scans were exclusively carried out under calm wind conditions (under  $4 \text{ m s}^{-1}$  in 16-scan plots, under  $8 \text{ m s}^{-1}$  in single scan  
161 plots) and in dry weather. The scanning heights ranged from 1.4 to 1.8 m above the ground. In plots that had 16 scan positions,  
162 co-registration of scans was done using 25 polystyrene sphere targets, mounted on 1.5-meter-tall sticks placed within the plot  
163 area (Fig. 2). The co-registration errors were below 1 cm. All processing was done with the Leica Cyclone software.

164 The point clouds are intended for spatial modeling of canopy structure based on ray tracing rather than morphological  
165 modeling. Therefore, no filtering was applied at any stage of the data processing to preserve information. The TLS data in  
166 plots with 16 scans are available as full-resolution data, with each individual scan's point cloud stored separately, along with  
167 the transformation parameters of the co-registration. For viewing purposes, we merged and downsampled the point clouds to  
168 an average point spacing of 2 cm in Leica Cyclone, and cropped the plot to approximately a  $35 \text{ m} \times 35 \text{ m}$  area for the plots  
169 that had 16 grid (scanning) points. For the single-scan plots, the downsampled point cloud includes all data. The downsampled  
170 and merged point clouds are provided in the LAS format.

171

### 172 **2.3.3 Hemispherical photographs**

173 We also obtained a characterization of the tree canopies with hemispherical photography. Hemispherical photographs were  
174 taken in each plot under diffuse illumination and windless or calm wind conditions with a Nikon D5000 digital camera  
175 equipped with a geometrically calibrated lens (Sigma EX 4.5 mm f/2.8 DC HSM). The photographs were captured from 21  
176 locations in each plot (Fig. 2) with the camera lens looking directly upwards. The camera was positioned at a height of 1.5 m  
177 when the mean tree height in a stand was over 10 m, and at a height of 1.0 m in other forests.

178 The photographs were recorded in the best quality eight-bit JPEG format. We manually adjusted the exposure time based on  
179 the illumination conditions and also took photographs with exposure times one stop higher and lower than the original, thus  
180 doubling and halving the exposure time. In the processing of the photographs, we selected the one where the pixel values in  
181 the blue band of the JPEG images filled the eight-bit dynamic range well without saturating the histogram, but also the other  
182 photographs are included in the dataset.

183 These hemispherical photographs served as the basis for estimating effective plant area index ( $\text{PAI}_{\text{eff}}$ ) and canopy gap fractions  
184 in different view angles. Initially, the JPEG photographs were binarized according to Nobis and Hunziker (2005). Next,  
185 effective PAI was calculated based on gap fractions determined for five concentric rings, each with median zenith angles of  
186  $10.7^\circ$ ,  $23.7^\circ$ ,  $38.1^\circ$ ,  $52.8^\circ$ , and  $66.6^\circ$ . This method closely followed the one presented in the manual of the LAI-2200 Plant  
187 Canopy Analyzer (LI-COR 2012), with minor variations in the zenith angles (as listed above). **The systematic uncertainties in  
188 the gap fractions estimated from hemispherical photographs are less than 0.02. This estimate is based on a comparison to the  
189 spectral canopy transmittance measured at 450 nm (Section 2.3.5).**

190

### 191 **2.3.4 Hyperspectral measurements and other characteristics of the forest floor**

192 We measured the spectral properties of the forest floor and estimated the fractional cover of different components forming the  
193 forest floor in all plots. The composition of the forest floor ranged from nearly bare soil or litter to dense green vascular or  
194 moss vegetation.

195 Hemispherical-conical reflectance factors (HCRF) of the forest floor (ranging from 350 to 2500 nm) were measured in a central  
196 location in each plot using an Analytical Spectral Devices (ASD) FieldSpec4 spectrometer (serial number 18456) with a 25°  
197 field-of-view. The initial spectral resolution ranged from 3 nm (for wavelengths ≤1000 nm) to 10 nm (for wavelengths >1000  
198 nm), the sampling interval was 1.4 nm and 1.1 nm for visible and near infrared (VNIR), and shortwave infrared (SWIR),  
199 respectively, and the instrument interpolated and outputted the data at 1 nm intervals. Please note that the same details on  
200 spectral resolution also apply to the data measured by the spectrometers described later in Sections 2.3.5 and 2.3.6.  
201 Measurements were consistently conducted under diffuse illumination conditions, so that the influence of unstable illumination  
202 conditions on the forest floor (i.e., sun flecks, shadows) could be avoided and the data collected at different latitudes and times  
203 of the day would be comparable. Preparations for the measurements included a warming-up period for the spectrometer lasting  
204 at least 30 minutes.

205 In each plot, we established a 11-meter-long East-West oriented transect and made a total of 15 measurements at approximately  
206 80 cm intervals along it (Fig. 2). Measurements were recorded in the nadir direction from a height of approximately 1.3 m.  
207 For calibration, white reference measurements of a 25 cm × 25 cm Spectralon panel (with a nominal reflectance of 99%) were  
208 conducted at both ends of the transect as well as at every third measurement point along the transect. Dark current  
209 measurements were taken at both ends of the transect. The integration time, offset and gain of the spectrometer were adjusted  
210 based on illumination conditions using automatic optimization.

211 Raw radiation signals (i.e., digital numbers, DN) were processed into hemispherical-conical reflectance factors (HCRF), and  
212 the 15 pointwise measurements were averaged to produce a single spectrum per forest plot. We calculated the HCRF for each  
213 measurement point by dividing the DN value of the forest floor by the DN value of the Spectralon panel and multiplied this  
214 ratio with the reflectance of the white reference panel. Dark current readings were subtracted from all DN values prior to the  
215 calculation. Because white reference readings were made at every third measurement point, we performed a linear interpolation  
216 (in time) of the white reference measurements to obtain a value for all measurement points. The preprocessed data are provided  
217 in the csv format. **We estimated that these measurements have an uncertainty of ~10% due to variation in illumination**  
218 **conditions.**

219 Fractional cover was defined as the fraction of ground covered by living or dead plant material or lichens in 1 m<sup>2</sup> vegetation  
220 quadrats. Fractional cover was estimated for all plots from nadir-view RGB (red, green, blue) photographs (four per plot) taken  
221 by a Nikon D5000 camera at every fourth spectral measurement point (at a height of 1.5 m) along the transect where spectral  
222 measurements were made. A wooden frame of 1 m × 1 m was placed at these measurement points, and the entire frame  
223 (vegetation quadrat) was included in the photograph. After field work, the photographs were processed to obtain estimates of  
224 fractional cover. The frame in each photograph was superimposed with a 10 × 10 grid, where each grid cell represented 1% of  
225 the total image area. The forest floor present in each grid cell was visually classified into one of the following classes: 1)  
226 vascular plants, 2) non-vascular plants (i.e., mosses), 3) lichen, 4) intact plant litter, or 5) decomposed plant litter. The criterion  
227 for selecting one of the classes was that it was the most abundant class in the grid cell. Finally, the fractional cover of each  
228 class in the photograph was determined by aggregating the grid cell specific results, and the average fractional cover of each  
229 forest floor class within a forest plot was determined by calculating the mean of fractional cover values across the four  
230 photographs.

### 231 **2.3.5 Hyperspectral measurements of canopy transmittance**

232 We conducted measurements of spectral transmittance of tree canopies (ranging from 350 to 2500 nm) in 8 plots in Hyytiälä,  
233 6 plots in Järvelja, 4 plots in Lanžhot, and 4 plots in Bílý Kříž. Spectral transmittance of a canopy was defined as the ratio of  
234 below-canopy spectral radiation flux to above-canopy spectral radiation flux.



235 For these measurements, we used two FieldSpec3 or -4 spectrometers and two identical cosine receptors (diffuser type, model  
236 A124505) manufactured by ASD. In each forest plot, spectral transmittance was measured at 49 locations (Fig. 2). The ASD  
237 FieldSpec4 spectrometer (serial number 18456) was consistently employed for measurements within the forest (i.e., below-  
238 canopy), whereas the ASD FieldSpec3 or -4 (serial number 18641 or 16089) served as reference spectrometer (i.e., above-  
239 canopy). For the above-canopy measurements, a tripod was used to affix the cosine receptor which was measuring at 15 second  
240 intervals in an open area within the study site (within <2 km distance from the plots). Measurements were conducted only  
241 under cloud-free conditions, with solar elevation angles ranging from 30° to 45°.

242 Preparations for the measurements included a warming-up period for the spectrometers lasting at least 30 minutes, automatic  
243 optimization of the spectrometers' integration time and gain settings, and an intercalibration of the two spectrometers. The  
244 intercalibration took place at the beginning and end of each measurement period (max 3 h 20 min). It involved placing the  
245 cosine receptors next to each other in an open area and conducting ten measurements, with each measurement comprising 30  
246 averaged spectra from both spectrometers.

247 After the field campaign, the data were processed into canopy spectral transmittance ( $T$ ) as

$$248 \quad T = \frac{f_{bc}s_{bc}}{f_{ac}s_{ac}} k, \quad (1)$$

249 where  $s_{bc}$  and  $s_{ac}$  are raw signal (DN) values recorded below and above canopy, respectively,  $k$  is the ratio of DNs measured  
250 by the two spectrometers under identical irradiance conditions (obtained from the intercalibration measurements), and  $f_{bc}$  and  
251  $f_{ac}$  are correction factors that take into account possible changes of the integration time (at wavelengths up to 1000 nm) or the  
252 detector gain (at wavelengths above 1000 nm) due to re-optimization of either of the spectrometers during the measurement  
253 period. Re-optimization was needed if signal saturation occurred, for example, when measuring before noon, as the solar  
254 irradiance increased towards noon. All quantities in the equation are wavelength- or detector-dependent. **We estimated that  
255 these measurements have an uncertainty of ~5% due to variation in clear-sky illumination conditions.**

256

### 257 2.3.6 Hyperspectral measurements of tree leaves and needles

258 We measured the directional-hemispherical reflectance factors (DHRF) and directional-hemispherical transmittance factors  
259 (DHTF) ranging from 350 to 2500 nm of leaves and needles for fifteen dominant tree species within the study sites, adding up  
260 to a total of 1314 samples. The two coniferous tree species that we sampled were Norway spruce (*Picea abies* (L.) H. Karst.)  
261 and Scots pine (*Pinus sylvestris* L.). The thirteen broadleaved tree species that we measured were common hazel (*Corylus*  
262 *avellana* L.) English oak (*Quercus robur* L.), European alder (*Alnus glutinosa* (L.) Gaertn.), European ash (*Fraxinus excelsior*  
263 L.), European aspen (*Populus tremula* L.), European hornbeam (*Carpinus betulus* L.), European Turkey oak (*Quercus cerris*  
264 L.), goat willow (*Salix caprea* L.), hedge maple (*Acer campestre* L.), littleleaf linden (*Tilia cordata* Mill.), silver birch (*Betula*  
265 *pendula* Roth), white poplar (*Populus alba* L.) and willows (*Salix* sp.). For simplicity, we will refer to leaves and needles  
266 collectively as foliage in the following text.

267 The foliage samples were measured in laboratory conditions using ASD RTS-3ZC integrating spheres which were equipped  
268 with a 10 W collimated halogen light source. The integrating sphere was coupled with an ASD spectrometer (FieldSpec3 serial  
269 number 16089, or FieldSpec4 serial number 18456 or 18641). Preparations for the measurements included a warming-up  
270 period for the spectrometer lasting at least 30 minutes.

271 In all study sites, visibly healthy foliage samples were obtained from both sun-exposed positions in the top-of-canopy and  
272 shaded positions in the bottom-of-canopy using professional tree climbers, towers or long pruning shears. After cutting a

273 branch from the tree, it was stored in a cool environment (with a maximum storage time of 12 hours), maintained with adequate  
274 watering, and foliage was removed from the branch immediately before the spectral measurements.

275 For coniferous trees, two age cohorts of needles were always sampled: current year (c0) and one-year-old (c1) needles. **The**  
276 **position on a branch, along with the color of the needles and bark of the shoot, are macroscopic criteria that were used to**  
277 **recognize c0 shoots and needles. c1 shoots were recognized by the presence of dead and partially shed bud scales at the base**  
278 **of the c0 shoot.** In Hyytiälä, Järvelja and Bílý Kříž, three trees representing each tree species were sampled, with three samples  
279 collected for each foliage class in each tree. This means that for all tree species, we sampled sun-exposed c0 and shaded c0  
280 foliage samples, and for conifers, we also sampled sun-exposed c1 and shaded c1 foliage classes. For less common broadleaved  
281 species in Järvelja (European ash, goat willow, littleleaf linden, common hazelnut, and unspecified willow), samples from  
282 one tree were obtained, and three sun-exposed c0 leaves were collected per tree species. In Lanžhot, one to four trees were  
283 selected for sampling. Each tree contributed one sample for every foliage class, including shaded c0 or sun-exposed c0.

284 For the duration of the spectral measurement of a sample in Hyytiälä, Järvelja and Bílý Kříž, the sample (i.e., a leaf or a set  
285 of 7-10 needles) was fixed in a custom-made sample holder (see Fig. 1 in Hovi et al., 2020 for sample holder design) that was  
286 then fastened to the integrating sphere. Needles were arranged in the sample holder with a spacing of 0.5–1 times the width of  
287 a single needle (as recommended by Yáñez-Rausell et al. 2014), and leaves were placed so that major veins were not included  
288 in the measured spot. In Lanžhot, leaves of broadleaved species were not attached to sample holders.

289 We conducted measurements of DHRF and DHTF on both sides of the sample (corresponding to adaxial and abaxial in  
290 broadleaved species), along with white reference measurements for both DHRF and DHTF. A photon trap was used in the  
291 reflectance measurements to assess stray light. Our white reference was a Spectralon panel with 99% nominal reflectance. The  
292 raw data were processed to derive leaf or needle DHRF and DHTF for all samples. For brevity, we denote DHRF with  $R$  and  
293 DHTF with  $T$  in the following equations:

$$294 R = \frac{s_R}{s_{ref,R}} \frac{1}{1 - P_{gap,R}} R_{ref}, \quad (2)$$

$$295 T = \left( \frac{s_T}{s_{ref,T}} - P_{gap,T} \right) \frac{1}{1 - P_{gap,T}} R_{ref}, \quad (3)$$

296 where  $s_R$  and  $s_T$  represent the raw signals (DN) obtained from the DHRF and DHTF measurements. Similarly,  $s_{ref,R}$  and  $s_{ref,T}$   
297 denote the DNs from the white reference measurements for DHRF and DHTF, respectively.  $R_{ref}$  indicates the reflectance of  
298 the white reference panel, while  $P_{gap,R}$  and  $P_{gap,T}$  denote the gap fractions in the sample. Before  $R$  was computed, stray light  
299 was first subtracted from  $s_R$  and  $s_{ref,R}$ . **DHRF includes specular reflection.**

300 For broadleaved species, the gap fraction was assigned a value of 0 in the above calculations. Coniferous samples, on the other  
301 hand, included gaps between needles, and thus, we determined the gap fractions using a digital film scanner (Epson Perfection  
302 V550, 800 dpi resolution). The detailed procedure for determination of gap fraction was done according to Hovi et al. (2020).  
303 Finally, to address a slight inherent bias in DHTF measurements with the ASD RTS-3ZC integrating sphere (reported by Hovi  
304 et al. 2020) and to ensure that the sum of DHRF and DHTF did not exceed one in the near-infrared (NIR) region, we  
305 implemented an empirical correction in which the DHTF spectra were multiplied with a correction factor of 0.945. **Maximum**  
306 **uncertainty in spectral measurements of foliage, in general, corresponds to the maxima of biological variation (Petibon et al.**  
307 **2021). For coniferous (non-flat) needles, the errors are approximately 4%-6% in DHRF and 10%-12% in DHTF (Yáñez-**  
308 **Rausell et al. 2014).**

309 For data users, we provide the spectra for all samples as well as analysis-ready datasets. The analysis-ready datasets contain i)  
310 the mean DHRF and DHTF spectra and their standard deviations for all tree species, canopy positions (top and bottom), needle

311 age classes (c0, c1) and study sites, and ii) plot-specific mean DHRF and DHTF spectra which have been weighted based on  
312 tree species and needle age class proportions (i.e., computed from i).

## 313 2.4 Airborne datasets

### 314 2.4.1 Hyperspectral data

315 We arranged flight campaigns in mid-July 2019 in Hyytiälä and Järvelja, and in early September 2019 in Lanžhot and Bílý  
316 Kříž (Table 1), representing green phenological conditions. Airborne hyperspectral measurements were collected across all  
317 study sites using the CASI-1500 and SASI-600 hyperspectral pushbroom sensors from Itres Ltd., Canada, mounted on a Cessna  
318 C208B aircraft which is part of the Flying Laboratory of Imaging Systems (FLIS) operated by the CzechGlobe Global Change  
319 Research Institute (Hanuš et al., 2023). The CASI-1500 covered visible (VIS) to NIR wavelengths (382 to 1052 nm), while  
320 the SASI-600 sampled NIR and shortwave-infrared (SWIR) wavelengths (958 to 2443 nm). Both sensors had a sampling  
321 interval and spectral resolution of 15 nm and underwent spectral and radiometric calibration prior to the flight campaigns in  
322 March 2019.

323 During the flight campaigns, the aircraft flew at an altitude of approximately 1 km above ground level. This yielded ground  
324 pixel sizes of 0.5 m (CASI) and 1.25 m (SASI). The CASI and SASI data were acquired in near-nadir observation geometry  
325 with a +/- 20° field-of-view. The flying azimuth direction closely matched the solar azimuth – the purpose of this was to reduce  
326 potential spectral differences within the same study site caused by reflectance anisotropy of forests in the solar principal plane.  
327 During acquisitions, the Sun zenith angle ranged from 37° to 60°, and flight lines overlapped by 60–80%.

328 The raw DN data from the hyperspectral sensors underwent initial radiometric correction with the RadCor software (version  
329 11) produced by Itres Ltd. Subsequently, geo-orthorectification was performed using GeoCor (version 5.6). The data were  
330 orthorectified to a surface model, which represents the top-of-canopy in vegetated areas, and the ground elevation elsewhere.  
331 Atmospheric correction was carried out with the ATCOR-4 software bundle (version 7.2.0 or 7.3.0), employing a database of  
332 atmospheric look-up tables generated with the MODTRAN5 radiative transfer code. In this correction, sensor measurements  
333 were adjusted for path and adjacency radiances. Inflight radiometric (vicarious) calibration was conducted for each site using  
334 a known bright reflectance target. Spectral bands highly affected by water vapor in the atmosphere (i.e., 895-1003 nm, 1092-  
335 1168 nm, 1302-1528 nm, and 1737-2038 nm) were nonlinearly interpolated and depended on local atmospheric conditions.  
336 The parameters used in the atmospheric correction were retrieved directly from the airborne hyperspectral data. However, for  
337 the Hyytiälä site, the parameters were estimated from the on-site Aeronet station (CIMEL sunphotometer). No topographic  
338 correction was applied. The data produced through this processing chain are provided as at-surface (also called top-of-canopy)  
339 hemispherical-directional reflectance factors (HDRF). We estimated that the uncertainty in the HDRF data (assessed as the  
340 deviation between the atmospherically corrected airborne data and the ground-measured spectra of reference targets) was less  
341 than 2% in all wavelengths.

342 Finally, we inspected the CASI and SASI data manually to remove clouds or cloud shadows from areas corresponding to our  
343 study plots. During the flights, clouds were intermittently present over Hyytiälä site and occasionally in Bílý Kříž site. The  
344 Lanžhot and Järvelja flights, on the other hand, had cloudless conditions. Nearest-to-nadir cloud-free data from a 100 m ×  
345 100 m area around each plot were extracted and serve as an analysis-ready dataset. In addition, data from the entire study sites  
346 are provided. These data cover approximately 4 km × 4 km areas in Hyytiälä and Järvelja, 2 km × 3 km in Lanžhot, and 2 km  
347 × 2 km in Bílý Kříž.

## 348 2.4.2 Laser scanning data (ALS)

349 Airborne laser scanning (ALS) data were collected simultaneously with the airborne hyperspectral data using a Riegl LMS-  
350 Q780 laser scanner (Riegl GmbH, Austria) mounted on the same Cessna aircraft. The laser scanner operated at a wavelength  
351 of 1064 nm, had a 0.25 mrad beam divergence, and a maximum scan zenith angle of 30°. The pulse density at the study plots  
352 was 48, 32, 10, and 9 pulses m<sup>-2</sup> in Hyttiälä, Järvelja, Lanžhot, and Bílý Kříž, respectively. The differences between sites  
353 stem from different overlap of flight lines. In Hyttiälä, the elevated pulse density was also partly due to repeated flight lines  
354 due to occasional cloud cover. The lowest absolute positional accuracy (RMS 27 cm) is associated with coordinates for off-  
355 nadir points acquired at the edges of the flight lines. The calculation of this accuracy is based on the performance of each  
356 component provided by manufacturer and an acquisition height of 1030 m above ground. The raw waveform data were  
357 processed into point cloud format using RiProcess (version 1.8.4), RiAnalyze (version 6.2.2), RiWorld (version 5.1.3), and  
358 GeoSysManager (version 2.0.8) software. We also computed raster digital elevation models with a pixel size of 1 m, by  
359 interpolating from the ground points classified with LASTools software. Similarly to the airborne hyperspectral data, analysis-  
360 ready data were extracted for a 100 m × 100 m area around each study plot, and the data are also provided for the entire study  
361 sites as original point clouds and denoised data. Denoised data were processed to filter out points originating from the sky (due  
362 to e.g., clouds) or false points under ground.

## 363 2.5 External field datasets

364 Field datasets from other sources, and relevant to physically-based remote sensing but not included in our campaigns, are  
365 available for the study sites. We have summarized these datasets in Table 2. They include 1) reflectance spectra of tree bark  
366 for boreal and temperate tree species, 2) additional data sets on optical properties of Norway spruce needles from the Czech  
367 study sites, and 3) forest meteorology, greenhouse gases, air quality and soil measurements from ICOS towers.

369 **Table 2.** Ancillary data sets relevant for RT modeling of forests available for the study sites from other projects.

Description of data set	Source
Stem bark reflectance spectra for boreal and temperate tree species	DOI: 10.17632/pwfxgzz5fj.2
Forest meteorology, greenhouse gases, air quality and soil measurements	
for Hyttiälä site	DOI: 10.23729/23dd00b2-b9d7-467a-9cee-b4a122486039
for Lanžhot site	<a href="https://meta.icos-cp.eu/objects/LaXYKv7nUEOYLD62wr43PK7H">https://meta.icos-cp.eu/objects/LaXYKv7nUEOYLD62wr43PK7H</a> (last access 11 April 2024)
for Bílý Kříž site	<a href="https://meta.icos-cp.eu/objects/Ru01KATyDlvqFkOzvB7eBcrY">https://meta.icos-cp.eu/objects/Ru01KATyDlvqFkOzvB7eBcrY</a> (last access 11 April 2024)
Optical properties of Norway spruce needles	DOI: 10.17632/vycrxc4vpz.1

370

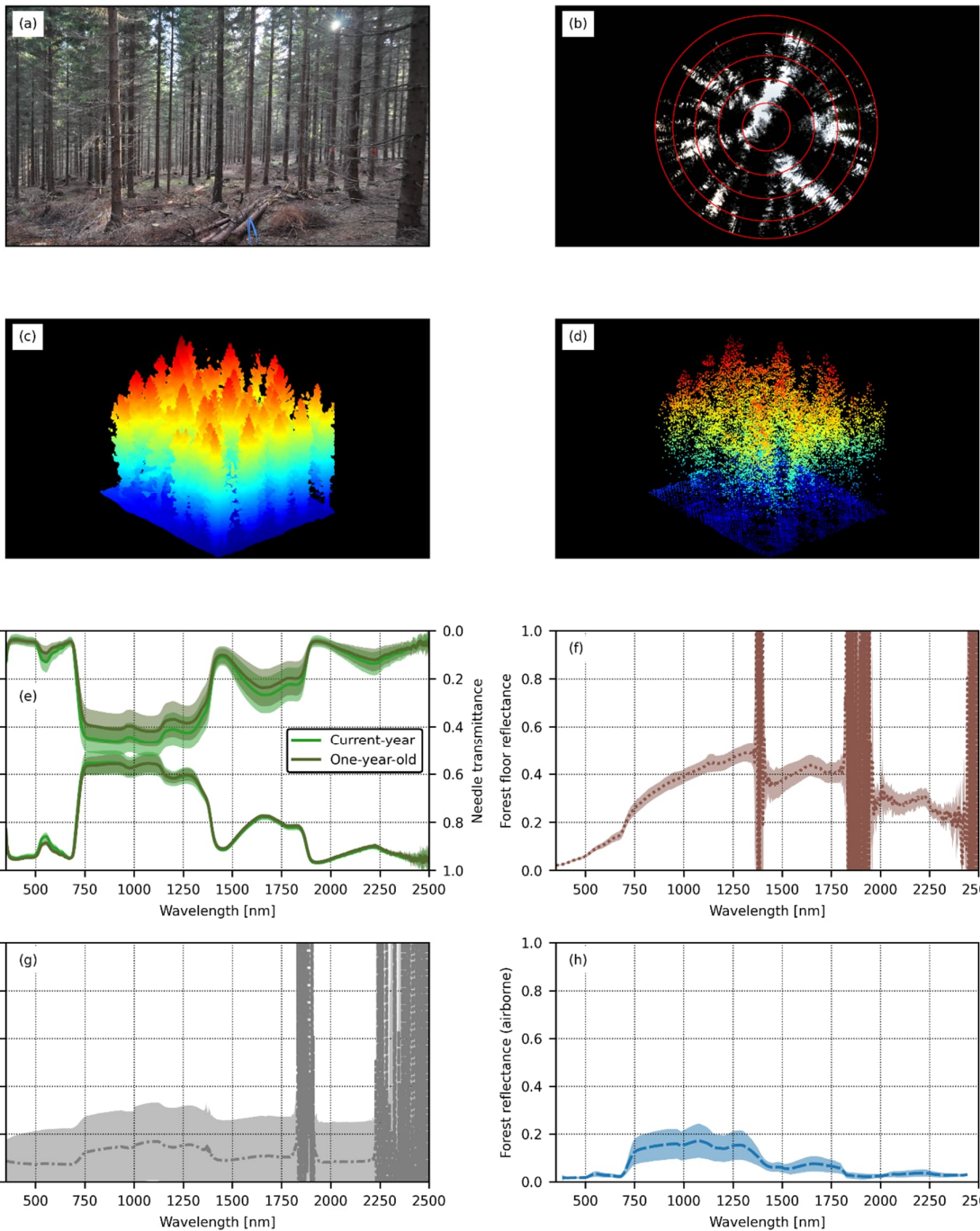
## 371 3 Results

372 The data allow examining comprehensively the spectral and structural properties of forest stands. We summarized the different  
373 data sources in two sets of figures, using a coniferous stand from Bílý Kříž (Fig. 3) and a broadleaved stand from Hyttiälä  
374 (Fig. 4) as examples. These two forest stands illustrate the variation in structural and spectral properties both within and  
375 between stands present in the new dataset. For example, the point clouds produced by laser scanning sensors and described in

376 this paper (Fig. 3c-d, 4c-d) can be used to visualize and compute canopy height distribution or density metrics, or to assess the  
377 spatial distribution patterns of trees or foliage clumping in the study stands. The variation in the spectral properties of the study  
378 stands, on the other hand, can be divided into several parts to examine tree leaf-level (Fig. 3e, Fig. 4e), forest floor level (Fig.  
379 3f, Fig. 4f) and tree canopy level (Fig. 3g-h, Fig. 4g-h) phenomena. As a specific example of a key structural variable needed  
380 in RT modeling of vegetation, we publish data on tree canopy gap fractions in different view angles based on hemispherical  
381 photography. On average, in our coniferous stands, canopy gap fractions were approximately two times as high as in the  
382 broadleaved stands, and in both types of forests, the gap fractions decreased linearly towards the horizon (Fig. 5).

383 Using the datasets described in this paper, differences in the spectral properties of forests can be investigated at multiple scales  
384 (Fig. 6). In presenting the data here, we refer to the spectral regions as visible (~400–700 nm), near infrared (~700–1300 nm)  
385 and shortwave infrared (~1300–2500 nm). In both coniferous and broadleaved stands, the reflectances were notably higher at  
386 tree leaf level than at stand (canopy) level throughout the entire measured spectrum (Fig. 6a-b). Forest floor reflectances, on  
387 the other hand, were usually lower than tree leaf level reflectances but higher than canopy level reflectances in the visible and  
388 near-infrared regions. However, in the shortwave infrared region, the forest floor had, on average, a higher reflectance than  
389 tree leaves or canopies in coniferous stands, and a reflectance similar to that of tree leaves in broadleaved stands (Fig. 6a-b).  
390 An especially unique feature of this dataset is that also transmittance spectra at leaf and canopy levels were measured so that  
391 they could be used in, for example, testing the performance of RT models. In our data, the canopy level spectral transmittance  
392 of coniferous stands was more stable throughout the spectrum than the canopy level transmittance of broadleaved stands, and  
393 that transmittances at leaf and canopy levels were usually lower in our coniferous study plots than in broadleaved study plots  
394 (Fig. 6c-d). Furthermore, the data show that in the visible region, the spectral transmittance at canopy level was higher than  
395 the spectral transmittance at leaf level. In the near-infrared and shortwave infrared regions, on the other hand, leaf level  
396 transmittances were higher than canopy level transmittances. An exception to this was in the coniferous stands in two spectral  
397 regions – around 1400–1500 nm and above ~1900 nm – where canopy level transmittances were again higher than leaf level  
398 transmittances. In broadleaved stands, the canopy spectral transmittances in shortwave infrared were higher than leaf level  
399 transmittances only in a small region around 1900–2000 nm.

400 Finally, the data also allow examining relationships between structural and spectral properties of forests through a combination  
401 of contemporaneous airborne laser scanning and hyperspectral data (Fig. 7). These data can be used to illustrate, for example,  
402 that, in the visible spectral region, forest reflectance decreased as a function of increasing canopy cover (defined as the first  
403 echo cover index in ALS data) across forest stands representing different biomes (Figs. 7a, c), but that in the near-infrared and  
404 shortwave infrared regions, broadleaved and coniferous stands with closed canopies (i.e., high canopy cover values) formed  
405 two distinct groups so that coniferous stands had notably lower HDRFs than broadleaved stands did (Figs. 7e, g). Similar  
406 phenomena were also observed in the relationships between forest reflectance and canopy height (defined as the 95th percentile  
407 of all canopy echoes) obtained from ALS data (Fig. 7b, d, f, h).

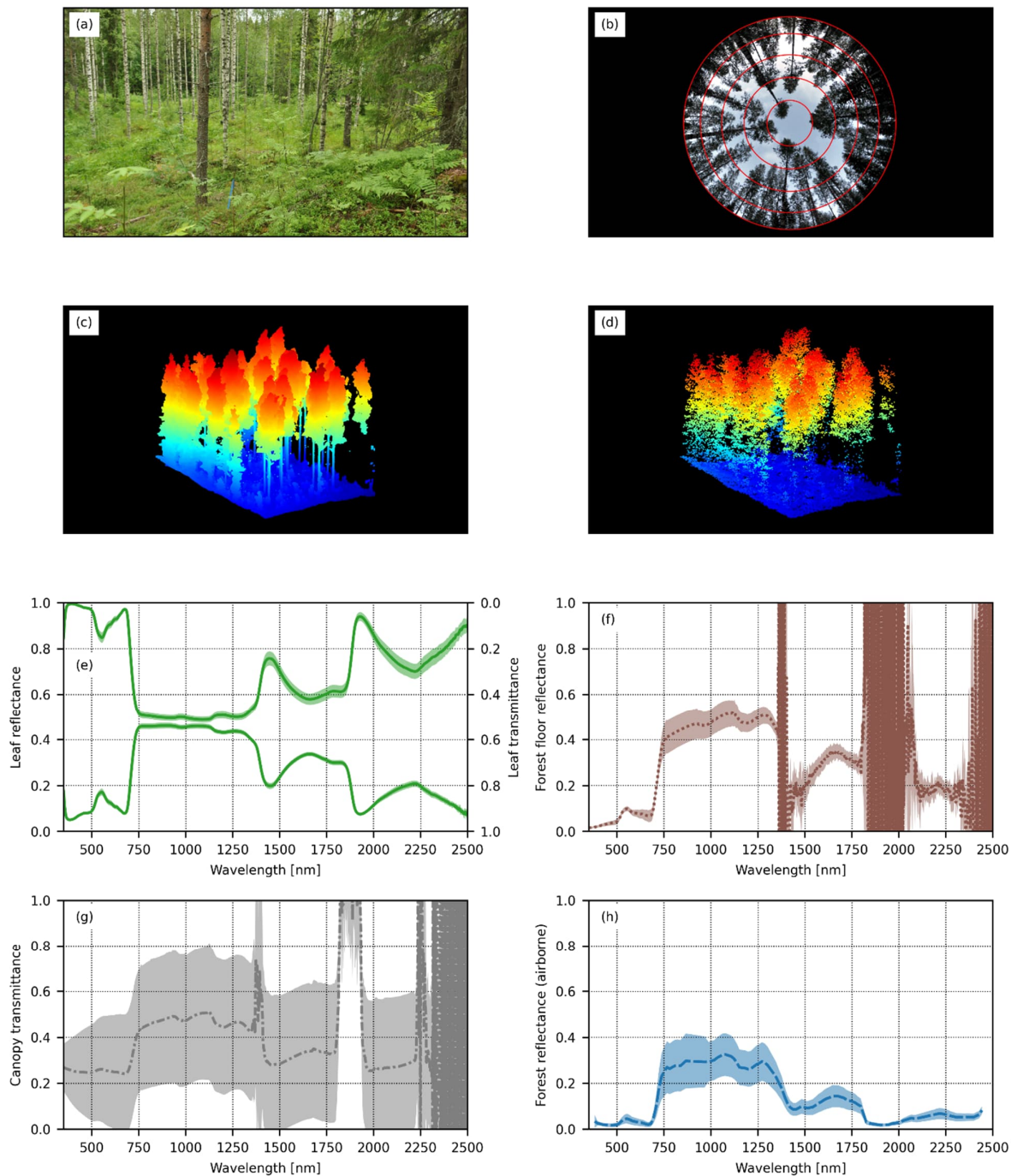


408

409 (figure caption continue on following page)

410 **Fig. 3.** A collection of figures summarizing the different types of data collected for a pure coniferous plot located in Bílý Kříž  
 411 (stand ID “BK\_SPRUCE2” in the dataset). The dominant tree species is Norway spruce (99% of basal area), effective plant  
 412 area index 2.8, and mean tree height 20.8 m. **A.** An overview photograph of the plot (from the north-east corner towards the  
 413 plot center). **B.** A hemispherical photograph of the canopy (Section 2.3.3). **C.** Point cloud visualization of the plot based on  
 414 terrestrial laser scanning data from the south-west corner towards the plot center based on a downsampled point cloud (Section  
 415 2.3.2). **D.** Point cloud visualization of the plot based on airborne laser scanning data from the south-west corner towards the  
 416 plot center (from view zenith angle  $45^\circ$ ,  $17 \text{ pulses m}^{-2}$ ) (Section 2.4.2). **E.** Mean leaf-level reflectance and transmittance spectra  
 417 (DHRF and DHTF, respectively) and their standard deviations for current year and one-year-old needles of the dominant tree  
 418 species in the plot (Section 2.3.6). **F.** Mean reflectance spectrum (HCRF) and its standard deviation for the forest floor in the  
 419 plot (Section 2.3.4). Spectral regions with noise were caused by atmospheric water vapor. **G.** Mean spectral transmittance and

420 its standard deviation for the tree canopy layer (Section 2.3.5). Spectral regions with noise were mainly caused by atmospheric  
 421 water vapor, but also by the reduced sensitivity of the cosine receptor at the end of the spectral range (>2200 nm). **H.** Mean  
 422 reflectance spectrum (HDRF) and its standard deviation for the entire plot (25 m × 25 m area) based on airborne measurements  
 423 (Section 2.4.1).

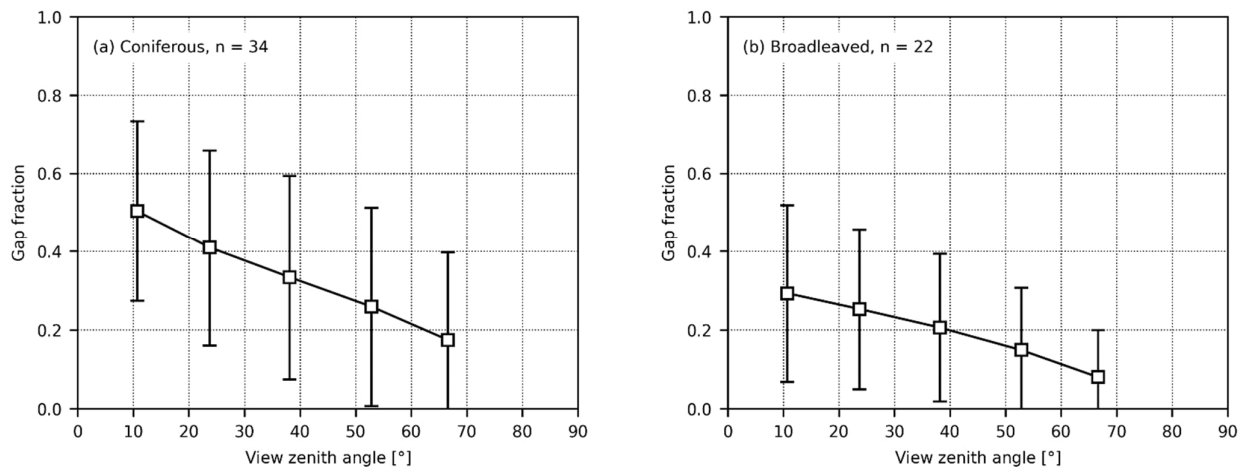


424

425 (figure caption continues on following page)

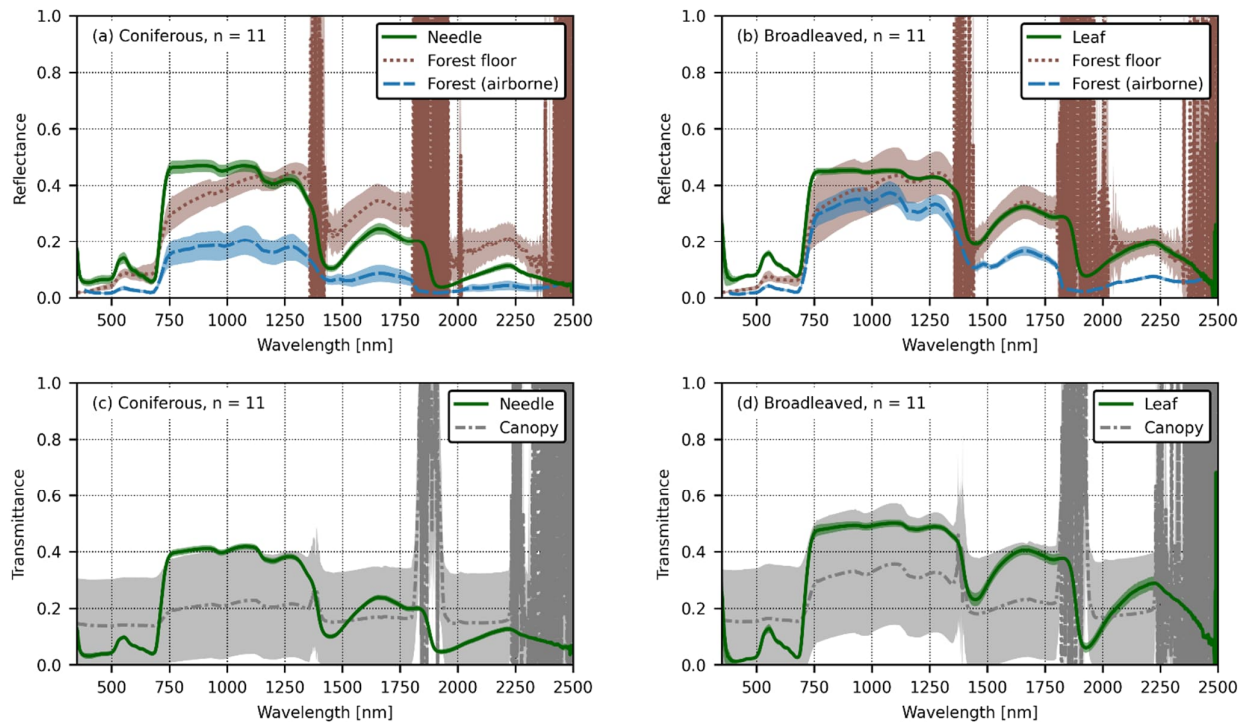
426 **Fig. 4.** A collection of figures summarizing the different types of data collected for a broadleaved plot located in Hyytiälä  
 427 (stand ID “HY\_BIRCH2” in the dataset). The dominant tree species is silver birch (85% of basal area), effective plant area  
 428 index 1.5, and mean tree height 23.2 m. **A.** An overview photograph of the plot (from the north-west corner towards the plot  
 429 center). **B.** A hemispherical photograph of the canopy (Section 2.3.3). **C.** Point cloud visualization of the plot based on

430 terrestrial laser scanning data from the south-west corner towards the plot center based on a downsampled point cloud (Section  
 431 2.3.2). **D.** Point cloud visualization of the plot based on airborne laser scanning data from the south-west corner towards the  
 432 plot center (from view zenith angle  $45^\circ$ ,  $48 \text{ pulses m}^{-2}$ ) (Section 2.4.2). **E.** Mean leaf-level reflectance and transmittance spectra  
 433 (DHRF and DHTF, respectively) and their standard deviations for the dominant tree species in the plot (Section 2.3.6). **F.**  
 434 Mean reflectance spectrum (HCRF) and its standard deviation for the forest floor in the plot (Section 2.3.4). Spectral regions  
 435 with noise were caused by atmospheric water vapor. **G.** Mean spectral transmittance and its standard deviation for the tree  
 436 canopy layer (Section 2.3.5). Spectral regions with noise were mainly caused by atmospheric water vapor, but also by the  
 437 reduced sensitivity of the cosine receptor at the end of the spectral range ( $>2200 \text{ nm}$ ). **H.** Mean reflectance spectrum (HDRF)  
 438 and its standard deviation for the entire plot ( $25 \text{ m} \times 25 \text{ m}$  area) based on airborne measurements (Section 2.4.1).  
 439  
 440  
 441

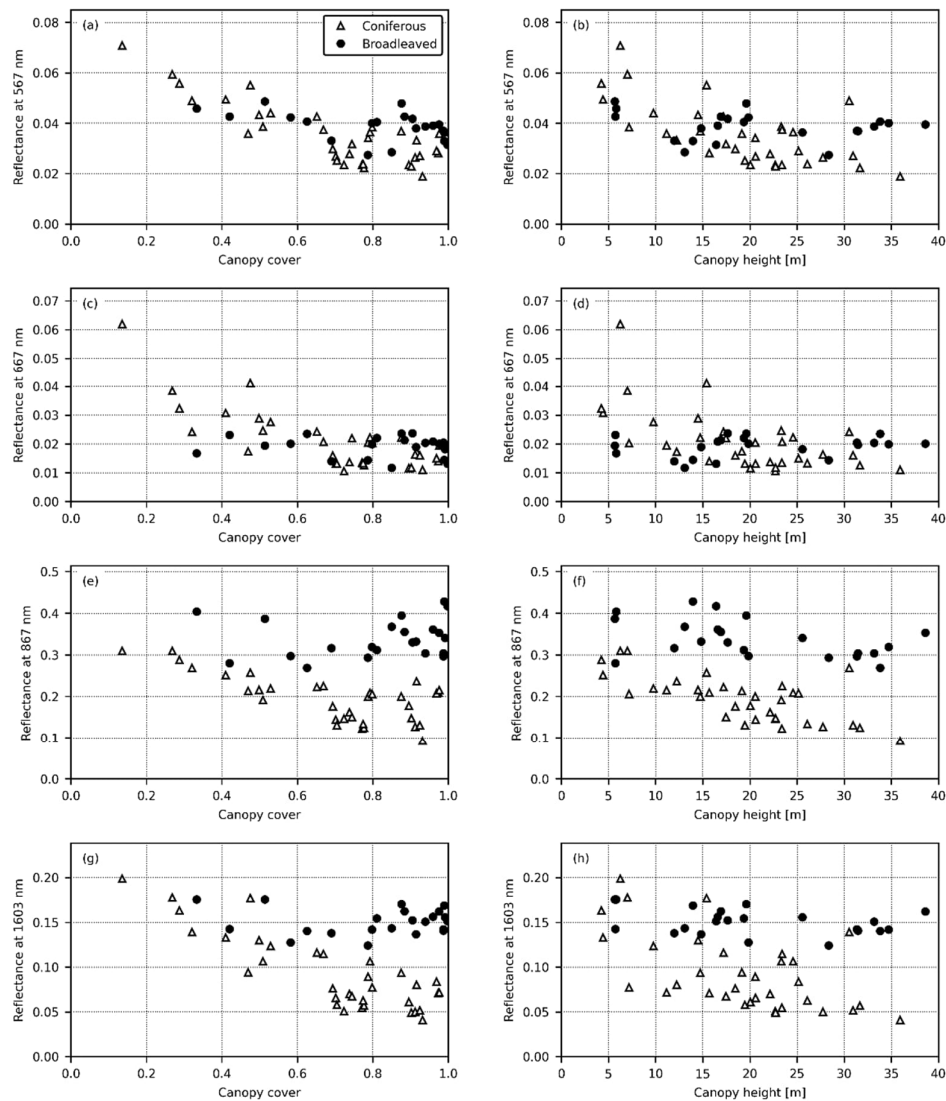


442  
 443 **Fig. 5.** Mean and standard deviation of canopy gap fractions in concentric view zenith angles as obtained from hemispherical  
 444 photographs in **A)** coniferous and **B)** broadleaved forests. Here, coniferous and broadleaved forests were defined so that at  
 445 least 75% of the trees (based on basal area) within the plot were coniferous or broadleaved species, respectively. The data  
 446 shown in this figure are based on measurements described in Section 2.2.3. (n = number of plots)





447  
 448 **Fig. 6.** Mean spectra at different scales. **A.** Mean reflectance spectra and their standard deviations for needles, forest floor and  
 449 entire forest plot in coniferous forests. **B.** Mean reflectance spectra and their standard deviations for leaves, forest floor and  
 450 entire forest plot in broadleaved forests. **C.** Mean transmittance spectra and their standard deviations for needles and canopies  
 451 in coniferous forests. **D.** Mean transmittance spectra and their standard deviations for needles and canopies in broadleaved  
 452 forests. The data shown in this figure are based on measurements and reflectance quantities described and defined in Sections  
 453 2.2.4-2.2.6 and 2.4.1., and only the subset of plots which had measurements of canopy transmittance are included here.  
 454 Coniferous and broadleaved forests were defined so that at least 75% of the trees (based on basal area) within the plot were  
 455 coniferous or broadleaved species, respectively. For visualization purposes, leaf-level reflectance and transmittance spectra  
 456 were first computed at plot-level as averages weighted by tree species proportions and needle age classes, and then averaged  
 457 over all plots to obtain the mean and standard deviation values shown in the above. Forest floor reflectance and canopy  
 458 transmittance data are shown with the noise that is inherently present in atmospheric water absorption bands in spectral data  
 459 measured outdoors. Forest reflectance (HDRF at plot-level, Fig. 6A and 6B) is averaged for an area of 25 m × 25 m in each  
 460 stand, and is based on airborne CASI and SASI data. (n = number of plots)



461  
 462 **Fig. 7.** The relationship between forest reflectance (HDRF, obtained from airborne CASI and SASI data) and forest structure  
 463 (obtained from ALS data, scan zenith angle max 20°) for broadleaved and coniferous forests in four spectral regions: green  
 464 (567 nm), red (667 nm), near-infrared (NIR, 867 nm) and shortwave infrared (SWIR, 1603 nm). The data are averaged for an  
 465 area of 25 m × 25 m in each stand. Canopy cover was defined as the first echo cover index in ALS data, so that first echoes  
 466 originating from the canopy were divided by all first echoes in the plot. **A. C. E. G.** Canopy cover and forest reflectance  
 467 (HDRF). Spectral region indicated on the y-axis. **B. D. F. H.** Canopy height (defined as the 95th percentile of all canopy echoes  
 468 in ALS data) and forest reflectance (HDRF). Spectral region indicated on the y-axis. Coniferous and broadleaved forests were  
 469 defined so that at least 75% of the trees (based on basal area) within the plot were coniferous or broadleaved species,  
 470 respectively. The data shown in this figure are based on measurements described in Section 2.4.

471 **4 Data availability**

472 The data are available in the open access repository Fairdata IDA which is a research data storage service provided by the  
 473 Ministry of Education and Culture of Finland. The data can be accessed at: Hovi et al. 2024a  
 474 <https://doi.org/10.23729/9a8d90cd-73e2-438d-9230-94e10e61adc9> (for data described in Section 2.3.) and Hovi et al. 2024b  
 475 <https://doi.org/10.23729/c6da63dd-f527-4ec9-8401-57c14f77d19f> (for data described in Section 2.4.).

476 **5 Conclusions**

477 Radiative transfer models of vegetation play a key role in advancing remote sensing science. The development of these models  
478 has been hindered by a lack of comprehensive ground reference data on both the structural and spectral characteristics of  
479 forests. In this paper, we introduced datasets containing information on the structural and spectral properties of temperate,  
480 hemiboreal, and boreal European forest stands. We anticipate that these data will have wide use in testing and validating  
481 radiative transfer models for forests and in other remote sensing studies beyond radiative transfer model development.  
482

483 **Author contributions**

484 MR, AH and DS conceptualized the scientific data collection plan for the project. AH, DS, PL, ZL, LH and MR organized the  
485 field campaigns and participated in data collection or processing. JH was responsible for organizing the airborne operations  
486 and related data processing. AH curated the datasets and prepared data visualizations. MR prepared the manuscript with  
487 contributions from all co-authors. MR was responsible for project administration and funding.  
488

489 **Competing interests**

490 The contact author has declared that none of the authors has any competing interests.  
491

492 **Acknowledgements**

493 We thank Juho Antikainen, Lucie Červená, Petri Forsström, Bijay Karki, Jussi Juola, Titta Majasalmi, Eva Neuwirthová, Ville  
494 Ranta and Jaan Rönkkö for field work or data processing; Jan Pisek, Mait Lang, Mihkel Kaha and Andres Kuusk for support  
495 in organizing the measurement campaign in Estonia; Jana Albrechtová for resources in organizing the field measurements in  
496 the Czech Republic; Karel Holouš, Lukáš Fajmon and Tomáš Fabiánek for participation and support in airborne operations;  
497 Lucie Hradecká and Ilari Lähteenmäki for advice in data management planning; and staff of all field stations of our study sites  
498 for their help at different stages of the work.  
499

500 **Financial support**

501 This study received funding from the European Research Council (ERC) under the European Union's Horizon 2020 research  
502 and innovation programme (grant agreement No 771049 / Rautiainen). The text reflects only the authors' view and the Agency  
503 is not responsible for any use that may be made of the information it contains. The work of the Czech scientists was made  
504 possible by the Ministry of Education of the Czech Republic, project LTAUSA18154: Assessment of ecosystem function  
505 based on Earth observation of vegetation quantitative parameters retrieved from data with high spatial, spectral and temporal  
506 resolution, and the CzeCOS program, grant number LM2023048.  
507  
508

509 **References**

- 510  
511 Fassnacht, F., White, J., Wulder, M. and Næsset, E.: Remote sensing in forestry: current challenges, considerations and  
512 directions. *Forestry: An International Journal of Forest Research*, 97(1), 11–37, <https://doi.org/10.1093/forestry/cpad024>,  
513 2024.
- 514 Gastellu-Etchegorry, J., Demarez, V., Pinel, V., and Zagolski, F.: Modeling radiative transfer in heterogeneous 3-D vegetation  
515 canopies. *Remote Sensing of Environment*, 58, 131–156, [https://doi.org/10.1016/0034-4257\(95\)00253-7](https://doi.org/10.1016/0034-4257(95)00253-7), 1996.
- 516 Gobron, N., Lanconelli, C., Urraca Valle, R. and Govaerts, Y.: RAMI workshop – Radiative transfer modelling support to EO  
517 metrology and Cal/Val activities. European Commission, Joint Research Centre, Publications Office of the European Union,  
518 <https://data.europa.eu/doi/10.2760/23274>, last access: 11 April 2024.
- 519 Hanuš, J., Slezák, L., Fabiánek, T., Fajmon, L., Hanousek, T., Janoutová, R.,Kopkáně, D., Novotný, J., Pavelka, K., Píkl, M.,  
520 Zemek, F., and Homolová, L.: Flying Laboratory of Imaging Systems: Fusion of Airborne Hyperspectral and Laser Scanning  
521 for Ecosystem Research. *Remote Sensing*, 15, 3130, <https://doi.org/10.3390/rs15123130>, 2023.
- 522 Hernández-Clemente, R., Homero, A., Möttus, M., Penuelas, J., González-Dugo, V., Jiménez, J., Suárez, L., Alonso, L., and  
523 Zarco-Tejada, P.: Early Diagnosis of Vegetation Health From High-Resolution Hyperspectral and Thermal Imagery: Lessons  
524 Learned From Empirical Relationships and Radiative Transfer Modelling, 5, 169–183, <https://doi.org/10.1007/s40725-019-00096-1>, 2019.
- 526 Hovi A., Möttus M., Juola J., Manoocheri F., Ikonen E., and Rautiainen M.: Evaluating the performance of a double integrating  
527 sphere in measurement of reflectance, transmittance, and albedo of coniferous needles. *Silva Fennica*, 54(2), 10270.  
528 <https://doi.org/10.14214/sf.10270>, 2020.
- 529 Hovi, A., Schraik, D., Hanuš, J., Lukeš, P., Lhotáková, Z., Homolová, L., and Rautiainen, M.: A spectral-structural  
530 characterization of European temperate, hemiboreal and boreal forests: Airborne data. [https://doi.org/10.23729/c6da63dd-  
531 f527-4ec9-8401-57c14f77d19f](https://doi.org/10.23729/c6da63dd-f527-4ec9-8401-57c14f77d19f), 2024b.
- 532 Hovi, A., Schraik, D., Hanuš, J., Lukeš, P., Lhotáková, Z., Homolová, L., and Rautiainen, M.: A spectral-structural  
533 characterization of European temperate, hemiboreal and boreal forests: Laboratory and field data.  
534 <https://doi.org/10.23729/9a8d90cd-73e2-438d-9230-94e10e61adc9>, 2024a.
- 535 Jacquemoud, S., Verhoef, W., Baret, F., Bacour, C., Zarco-Tejada, P., Asner, G., François, C., and Ustin, S.: PROSPECT +  
536 SAIL models: A review of use for vegetation characterization. 113, S1, S56-S66, <https://doi.org/10.1016/j.rse.2008.01.026>,  
537 2009.
- 538 Kooistra, L., Berger, K., Brede, B., Graf, L. V., Aasen, H., Roujean, J.-L., Machwitz, M., Schlerf, M., Atzberger, C., Prikaziuk,  
539 E., Ganeva, D., Tomelleri, E., Croft, H., Reyes Muñoz, P., Garcia Millan, V., Darvishzadeh, R., Koren, G., Hermann, I.,  
540 Rozenstein, O., Belda, S., Rautiainen, M., Rune Karlsen, S., Figueira Silva, C., Cerasoli, S., Pierre, J., Tanır Kayıkçı, E.,  
541 Halabuk, A., Tunc Gormus, E., Fluit, F., Cai, Z., Kycko, M., Udelhoven, T., and Verrelst, J.:Reviews and syntheses: Remotely  
542 sensed optical time series for monitoring vegetation productivity, *Biogeosciences*, 21, 473–511, [https://doi.org/10.5194/bg-  
543 21-473-2024](https://doi.org/10.5194/bg-21-473-2024), 2024.
- 544 Kuusk, A., Kuusk, J. and Lang, M.: A dataset for the validation of reflectance models. *Remote Sensing of Environment*, 113(5),  
545 889–892, <https://doi.org/10.1016/j.rse.2009.01.005>, 2009.
- 546 Kuusk, A. and Nilson, T.: A directional multispectral forest reflectance model. *Remote Sensing of Environment*, 72, 244–252,  
547 [https://doi.org/10.1016/S0034-4257\(99\)00111-X](https://doi.org/10.1016/S0034-4257(99)00111-X), 2000.
- 548 Leblanc, S. and Chen, J.: A windows graphic user interface (GUI) for the five-scale model for fast BRDF simulations. *Remote  
549 Sensing Reviews*, 19, 293–305, <https://doi.org/10.1080/02757250009532423>, 2000.
- 550 Liang, S.: Canopy reflectance modeling. In: *Quantitative remote sensing of land surfaces*. Wiley, New Jersey, USA, 76–134,  
551 ISBN: 0-471-28166-2, 2004.
- 552 LI-COR 2012. LAI-2200 plant canopy analyzer instruction manual. LI-COR, Inc., publication number 984-10633, rev 2.  
553 <https://www.licor.com/documents/6n3conpja6uj9aq1ruyn>, last access: 11 April 2024.
- 554 Luoma, V., Saarinen, N., Wulder, M., White, J., Vastaranta, M., Holopainen M. and Hyypä, J.: Assessing Precision in  
555 Conventional Field Measurements of Individual Tree Attributes. *Forests*, 8(2), 38, <https://doi.org/10.3390/f8020038>, 2017.
- 556 Malenovský, Z., Homolová, L., Lukeš, P., Buddenbaum, H., Verrelst, J., Alonso, L., Schaeppman, M., Lauret, N. and  
557 Gastellu-Etchegorry, J.: Variability and Uncertainty Challenges in Scaling Imaging Spectroscopy Retrievals and Validations  
558 from Leaves Up to Vegetation Canopies. *Surveys in Geophysics*, 40, 631–656, <https://doi.org/10.1007/s10712-019-09534-y>,  
559 2019.
- 560 Myneni, R. and Ross, J.: *Photon-vegetation interactions: Applications in optical remote sensing and plant ecology*. Springer-  
561 Verlag, Berlin, Heidelberg, Germany. 565 pp., ISBN: 978-3-642-75391-6, 1991.
- 562 NEON (National Ecological Observatory Network): <https://www.neonscience.org/>, last access: 11 April 2024.
- 563 Nobis, M. and Hunziker, U.: Automatic thresholding for hemispherical canopy-photographs based on edge detection.  
564 *Agricultural and Forest Meteorology*, 128(3-4), 243–250, <https://doi.org/10.1016/j.agrformet.2004.10.002>, 2005.
- 565 North, P.: Three-dimensional forest light interaction model using a Monte Carlo method. *IEEE Transactions on Geoscience*

566 and Remote Sensing, 34(4), 946 – 956, doi: [10.1109/36.508411](https://doi.org/10.1109/36.508411), 1996.

567 Petibon, F., Czyż, E., Ghielmetti, G., Hueni, A., Kneubühler, M., Schaepman, M. and Schuman, M.: Uncertainties in  
568 measurements of leaf optical properties are small compared to the biological variation within and between individuals of  
569 European beech. *Remote Sensing of Environment*, 264, 11260, doi: <https://doi.org/10.1016/j.rse.2021.112601>, 2021.

570 Pettorelli, N., Wegmann, M., Skidmore, A., Mücher, S., Dawson, T.P., Fernandez, M., Lucas, R., Schaepman, M.E., Wang,  
571 T., O'Connor, B., Jongman, R.H.G., Kempeneers, P., Sonnenschein, R., Leidner, A.K., Böhm, M., He, K.S., Nagendra, H.,  
572 Dubois, G., Fatoyinbo, T., Hansen, M.C., Paganini, M., de Klerk, H.M., Asner, G.P., Kerr, J.T., Estes, A.B., Schmeller, D.S.,  
573 Heiden, U., Rocchini, D., Pereira, H.M., Turak, E., Fernandez, N., Lausch, A., Cho, M.A., Alcaraz-Segura, D., McGeoch,  
574 M.A., Turner, W., Mueller, A., St-Louis, V., Penner, J., Vihervaara, P., Belward, A., Reyers, B. and Geller, G.N.: Framing the  
575 concept of satellite remote sensing essential biodiversity variables: challenges and future directions. *Remote Sensing in  
576 Ecology and Conservation*, 2(3), 122-131, <https://doi.org/10.1002/rse2.15>, 2016.

577 Piao, S., Wang, X., Park, T., Chen C., Lian, X., He, Y., Bjerke, J., Chen, A., Ciais, P., Tommervik, H., Nemani, R. and Myneni,  
578 R.: Characteristics, drivers and feedbacks of global greening. *Nature Reviews Earth & Environment*, 1, 14–27,  
579 <https://doi.org/10.1038/s43017-019-0001-x>, 2020.

580 Ross, J.: The radiation regime and architecture of plant stands. Kluwer Academic Publishers, The Hague, the Netherlands, 391  
581 pp., ISBN: 9061936071, 1981.

582 Schaepman-Strub, G., Schaepman, M., Painter, T., Dangel, S. and Martonchik, J.: Reflectance quantities in optical remote  
583 sensing—definitions and case studies. *Remote Sensing of Environment*, 103(1): 27-42,  
584 <https://doi.org/10.1016/j.rse.2006.03.002>, 2006.

585 Schneider, F.D., Morsdorf, F., Schmid, B., Petchey, O., Hueni, A., Schimel, D. and Schaepman, M.: Mapping functional  
586 diversity from remotely sensed morphological and physiological forest traits. *Nature Communications*, 8:1441.  
587 <https://doi.org/10.1038/s41467-017-01530-3>, 2017.

588 Sellers, P., Hall, F., Kelly, R., Black, A., Baldocchi, D., Berry, J., Ryan, M., Ranson, J., Crill, P., Lettenmaier, D.,  
589 Margolis, H., Cihlar, J., Newcomer, J., Fitzjarrald, D., Jarvis, P., Gower, S., Halliwell, D., Williams, D., Goodison, B.,  
590 Wickland, D. and Guertin, F.: BOREAS in 1997: Experiment overview, scientific results, and future directions. *Journal of  
591 Geophysical Research: Atmospheres*, 102(D24), 28731-28769, <https://doi.org/10.1029/97JD03300>, 1997.

592 Stenberg, P., Möttus, M. and Rautiainen, M.: Modeling the spectral signature of forests: application of remote sensing models  
593 to coniferous canopies. In (Ed. S. Liang): *Advances in Land remote Sensing: System, Modeling, Inversion and Application*.  
594 Springer-Verlag, 147-171, ISBN: 978-1-4020-6449-4, 2008.

595 Stenberg, P., Möttus, M. and Rautiainen, M.: Photon recollision probability in modelling the radiation regime of canopies —  
596 A review. *Remote Sensing of Environment*, 183, 98-108, <https://doi.org/10.1016/j.rse.2016.05.013>, 2016.

597 Verhoef, W.: Light scattering by leaf layers with application to canopy reflectance modeling: The SAIL model. *Remote  
598 Sensing of Environment*, 16(2), 125-141, [https://doi.org/10.1016/0034-4257\(84\)90057-9](https://doi.org/10.1016/0034-4257(84)90057-9), 1984.

599 Vicent, J., Sabater, N., Tenjo, C., Acarreta, J., Ramón, J., Manzano, M., Rivera, J. Jurado, P. Franco, R. Alonso, L., Verrelst,  
600 J., and Moreno, J.: FLEX End-to-End Mission Performance Simulator. *IEEE Transactions on Geoscience and Remote Sensing*,  
601 54(7), 4215-4223. doi: [10.1109/TGRS.2016.2538300](https://doi.org/10.1109/TGRS.2016.2538300), 2015.

602 Widłowski, J.-L., Mio, C., Disney, M., Adams, J., Andredakis, I., Atzberger, C., Brennan, J., Busetto, L., Chelle, M.,  
603 Ceccherini, G., Colombo, R., Côté, J.-F., Eemäe, A., Essery, R., Gastellu-Etchegorry, J. P., Gobron, N., Grau, E., Haverd, V.,  
604 Homolová, L., Huang, H., Hunt, L., Kobayashi, H., Koetz, B., Kuusk, A., Kuusk, J., Lang, M., Lewis, P., Lovell, J. L.,  
605 Malenovsky, Z., Meroni, M., Morsdorf, F., Möttus, M., Ni-Meister, W., Pinty, B., Rautiainen, M., Schlerf, M., Somers, B.,  
606 Stuckens, J., Verstraete, M. M., Yang, W., Zhao, F. and Zenone, T.: The fourth phase of the radiative transfer model  
607 intercomparison (RAMI) exercise: Actual canopy scenarios and conformity testing. *Remote Sensing of Environment*, 169,  
608 418-437, <https://doi.org/10.1016/j.rse.2015.08.016>, 2015.

609 Wilkinson, M.D., Dumontier, M., Aalbersberg, I.J.J., Appleton, G., Axton, M., Baak, A., Blomberg, N., Boiten, J.-W., Da  
610 Silva Santos, L.B., Bourne, P.E., Bouwman, J., Brookes, A.J., Clark, T., Crosas, M., Dillo, I., Dumon, O., Edmunds, S., Evelo,  
611 C.T., Finkers, R., Gonzalez-Beltran, A., Gray, A.J.G., Groth, P., Goble, C., Grethe, J.S., Heringa, J., Hoen, P.A.C., Hooft, R.,  
612 Kuhn, T., Kok, R., Kok, J., Lusher, S.J., Martone, M.E., Mons, A., Packer, A.L., Persson, B., Rocca-Serra, P., Roos, M., Van  
613 Schaik, R., Sansone, S.-A., Schultes, E., Sengstag, T., Slater, T., Strawn, G., Swertz, M.A., Thompson, M., Van Der Lei, J.,  
614 Van Mulligen, E., Velterop, J., Waagmeester, A., Wittenburg, P., Wolstencroft, K., Zhao, J. and Mons, B.: The FAIR Guiding  
615 Principles for scientific data management and stewardship. *Scientific Data*, 3, 160018. <https://doi.org/10.1038/sdata.2016.18>,  
616 2016.

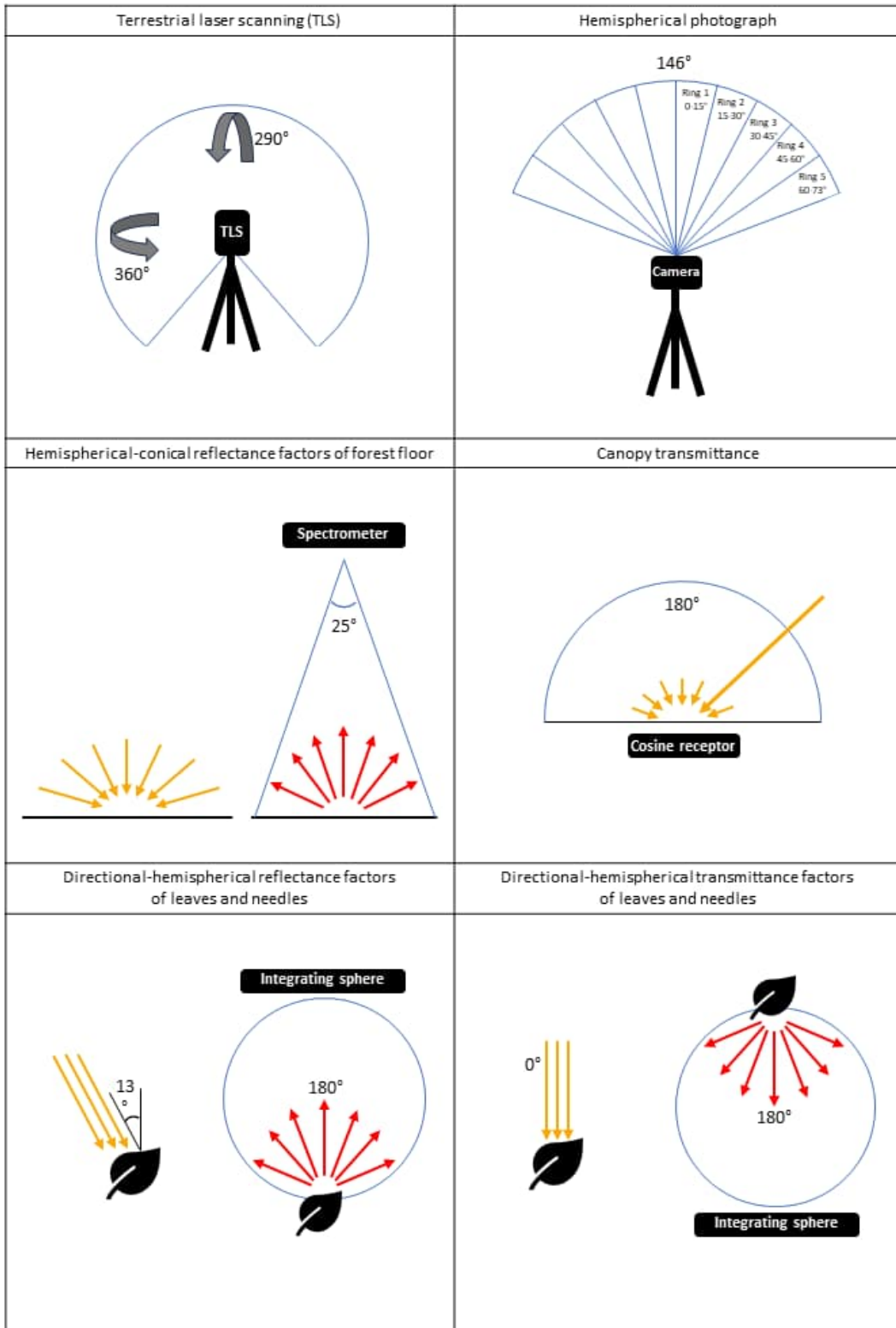
617 Yáñez-Rausell, L., Schaepman, S., Clevers, J. and Malenovsky, Z.: Minimizing Measurement Uncertainties of Coniferous  
618 Needle-Leaf Optical Properties, Part I: Methodological Review. *IEEE Journal of Selected Topics in Applied Earth  
619 Observations and Remote Sensing*, 7(2), 399-405, doi: [10.1109/JSTARS.2013.2272890](https://doi.org/10.1109/JSTARS.2013.2272890), 2014.

620

Appendix A



**Figure A1.** Photographs of different types of measurements conducted during the campaigns. **A.** Forest inventory measurements. **B.** Terrestrial laser scanning (TLS). **C.** Spectral transmittance reference measurements in an open place. **D.** Forest floor spectral measurements. **E.** Laboratory measurements of the spectral properties of foliage. **F.** Needle carriers used in the spectral measurements of foliage. **G.** Cessna 208B Grand Caravan aircraft used in the airborne campaigns. **H.** View of the sensors inside the Cessna aircraft.



664  
 665 **Figure A2.** Schemata showing the illumination and view geometries during the collection of field and laboratory data (Section  
 666 2.3).